Structure, Properties, and Phase Transitions of Melt-Spun Poly(vinylidene fluoride) Fibers

W. Steinmann,[1] S. Walter,[1] G. Seide,[1] T. Gries,[1] G. Roth,[2] M. Schubnell[3]

[1]Institut für Textiltechnik der RWTH Aachen (ITA), 52056 Aachen, Germany
[2]Institut für Kristallographie, RWTH Aachen (XTAL), 52056 Aachen, Germany
[3]Mettler Toledo GmbH, Sonnenbergstrasse 74, 8603 Schwerzenbach, Switzerland

ABSTRACT: Three different experimental techniques were used to study structural phase transitions in melt-spun poly(vinylidene fluoride) fibers, which were produced with different process parameters and processed in the draw-winding process at different temperatures and draw ratios. The fibers are examined with the help of wide-angle X-ray diffraction at elevated temperatures, differential scanning calorimetry with stochastic temperature modulation, and dynamic mechanical analysis. An oriented mesophase and deformed crystal structures can be observed in all fibers and assigned to the mechanical stress occurring in the processes. Furthermore, several phase transitions during melting and two mechanical relaxation processes could be detected. The observed transitions affect the crystal geometry, the orientation distribution, anisotropic thermal expansion, and the mechanic response of the fiber samples. The relaxation processes can be related with an increasing amount of crystalline β-phase in fibers drawn at different temperatures. The detailed information about phase transitions and the related temperatures are used to produce fibers with an extended amount of β-phase crystallites, which are responsible for piezoelectric properties of the material. © 2010 Wiley Periodicals, Inc. J Appl Polym Sci 120: 21–35, 2011

Key words: poly(vinylidene fluoride); fiber; phase transition

INTRODUCTION

Poly(vinylidene fluoride) (PVDF) is a fluoropolymer with the monomer unit CF_2–CH_2, with excellent chemical stability having a large dipole moment of 9.8×10^{-30} C m perpendicular to the polymer chain.[1,2] The material is processed to melt-blown films and melt-spun fibers.[3–5] Fibrous PVDF exists in monofilament and multifilament yarns.[6,7] One of the most interesting facts about the material is the piezoelectric, pyroelectric, and ferroelectric properties because of the existence of a polar crystal phase.[1,8] Piezoelectric PVDF films are commercially available and are used as actuators and sensors in many fields.[9,10]

Crystal structures

PVDF is a polymorphic material showing four well-known crystal phases at different processing conditions.[1,11] The nonpolar α phase, or Form II, with TGTG′ conformation (T = trans, G = gauche, G′ = antigauche) crystallizes from the melt having a monoclinic unit cell and showing a spherulitic morphology.[12,13] Experiments show that this phase is mainly formed in melt-spun fibers having a process-dependent orientation of the polymer chains along the fiber axis.[14] The polar δ or α_P phase (Form II_P) has the same geometry and forms in electric fields by rotating one of the chains in the unit cell.[15] The γ phase (or Form III) with TGTTTG′ conformation and monoclinic unit cell is formed by heat treatment at high temperatures or when casted from solution.[16,17] The polar β phase with all-trans conformation shows an orthorhombic unit cell.[16] This phase is formed under mechanical stress or high electric fields and is responsible for the ferroelectricity and piezoelectricity of the material.[11,18,19] The properties of the crystal structures are summarized in Table I.

Melt spinning

The production of synthetic fibers can be realized by thermoplastic extrusion or solution-based processes. Solution spinning is used for polymers that cannot be processed by thermoplastic melt extrusion mainly due to the fact that these polymers would start to degrade partially or completely before melting. PVDF is being spun by melt spinning and solution spinning.

TABLE I
Crystal Forms of Poly(vinylidene fluoride) and Their Properties[8]

Phase	α	β	γ	δ
Molecular conformation	TGTG′	TT	TTTGTTTG′	TGTG′
Space group	$P2_1/c\text{-}C_{2h}$	$Cm2n\text{-}C_{2v}$	$Cc\text{-}C_s$	$P2_1cn$
Lattice parameters	$a = 4.96$ Å; $b = 9.64$ Å; $c = 4.62$ Å; $\beta = 90°$	$a = 8.58$ Å; $b = 4.91$ Å; $c = 2.56$ Å	$a = 4.96$ Å; $b = 9.58$ Å; $c = 9.23$ Å; $\beta = 92.9°$	$a = 4.96$ Å; $b = 9.64$ Å; $c = 4.62$ Å; $\beta = 90°$
General formation	From melt	Mechanical stress/high electric field	Heat treatment; cast from solution	Electric field

Solution spinning of PVDF fibers leads to rather porous surfaces, which are utilized for membrane and filter applications. Melt spinning leads to fibers comparable to standard thermoplastic synthetic fibers, e.g., polyamide or polyester filaments. Cooling of as-spun fibers is realized either by air quenching or liquid bath. Usually, air quenching is the common method for rather fine fibers. Fibers with coarser diameters—generally referred to as monofilaments—are spun into a liquid (water or oil) bath.[20]

The fineness of filaments (or textile titer) T is commonly measured in dtex (decitex), which is a linear density indicating the mass in grams per 10,000 m. This unit is used for yarns made from both single and multiple filaments (multifilaments). In the case of multifilaments, the fineness of the whole yarn consisting of n filaments is indicated in dtex, and the fineness of a single filament is indicated in dpf (dtex per filament). If the density ρ of the polymer is known, the filament diameter D can be calculated from the fineness[20]:

$$D = 2\sqrt{\frac{T}{\pi n \rho}}$$

In this study, we examined the properties of PVDF multifilaments, which are melt extruded through multiple capillaries. After the solidification of the filaments, they are combined to the multifilament yarn. In general, multifilaments are spun 10 to 100 times faster than monofilaments with an increased melt draw ratio by this factor.[20]

Structure formation and crystalline properties of PVDF fibers were previously examined in monofilaments with diameters greater than 100 μm and spun at low take-up velocities between 20 and 200 m/min, showing the formation of an oriented α phase.[14] The formation of β-phase crystals is only achieved by spinning into a tempered liquid bath.[21] In the case of melt-blown films, the β phase is formed by drawing, where mechanical stress occurs.[22] Analog experiments show that drawing is also responsible for the β formation in fibers.[14,23] The temperature-dependent results from those of films or monofilaments cannot be transferred directly because pro-

duction and processing conditions differ massively in the case of high-speed melt spinning of multifilaments. Furthermore, there has been no proof of piezoelectricity in fibrous PVDF yet.

Application of multifilaments

Multifilaments can be produced as a textile yarn for clothing applications, where the materials polyamide (nylon) or polyester are in common use. Another possibility is the production of technical yarn used in filters, automotive applications like airbags or tires, geotextiles, or protective clothing. Textile multifilament yarn, which is part of this study, usually has smaller fiber diameters than technical yarn. Normally, the yarns are further processed by texturing, where a crimp is applied to the yarn. This crimp leads to a softer touch of the yarn and decreases its air permeability and thermal conduction.[20] In this study, we have focused only on the examination of flat yarns, since the examination of polymer chain orientation becomes difficult when it is superposed by the yarn crimp. For the given different applications, the yarn is converted to textile fabrics, which can be woven, warp knitted, or nonwoven.[20,24]

Aim of the study

Beyond the research of the technical production process, our aim was to understand the crystallization and phase transitions in PVDF fibers to optimize the formation of the β phase for further examination of the piezoelectric effect in fibers. The analysis of the produced and processed fibers was carried out with three different experimental techniques: wide-angle X-ray diffraction (WAXD) with measurements at elevated temperatures, differential scanning calorimetry (DSC) with temperature-modulated heating, and dynamic mechanical analysis (DMA). Each of these methods shows different aspects of phase transitions in the material and the corresponding changes at the molecular scale. Furthermore, only the combination of the techniques reveals important information to clearly identify the phases involved in the observed transitions.

EXPERIMENTAL

Material

The material used for fiber production, processing, and analysis is the PVDF homopolymer SOLEF 1006. The polymer with very low viscosity, a melt flow index (MFI) of 40 g/10 min at 230°C, and mass of 2.16 kg was chosen because of the best processability in melt spinning. The melting point and crystallization point of the raw material are specified as 175 and 138°C, respectively.[25]

Fiber production

Melt spinning

Melt spinning is the classical way of thermoplastic processing of polymers to fiber materials. The polymer in granule form is being transported into an extruder, where the polymer is compressed and through friction and increasing pressure among the granules melted. The melt exits the extruder at pressure levels around 80–110 bar and is transported through heated pipes to the spin pump. Up to the spin pump, the process and throughput are pressure controlled depending on the lead pressure at the extruder head. From the spin pump on, it is a throughput-controlled process. The polymer is pumped into the spin pack, which consists of multiple filtration layers. These can be woven metal structures, ceramic, or metallic nonwovens, and also stainless steel sand is commonly in use for melt spinning. After passing through all filtration stages, the melt flows into the capillaries of the spinneret. At the end of the capillary, the melt exits and forms a fiber. The temperature of the extrusion equipment and thus the melt are the major process parameters determining the viscosity and shearing of the polymer. For PVDF, a flat profile with little increase of temperature is set from extruder feeding to spinneret. The extrusion temperature is chosen at 260°C, where polymer viscosity is low enough to allow a stable processing. Mass flow rate Q is controlled by the spinning pump and adjusted to 59.5 g/min. With the help of the total capillary area in the spinning plate

$$A = n\pi \left(\frac{D_0}{2}\right)^2,$$

the density ρ and the extrusion velocity v_e can be calculated:

$$v_e = \frac{Q}{\rho A}$$

Over a length of 1500 mm, the filaments are cooled by a laminar air stream at 21°C perpendicular to the fiber axis. The as-spun fibers are drawn down

TABLE II
Melt Spinning Parameters for PVDF Fiber Production

Parameter	Value
Number of filaments (n)	34
Capillary diameter (D)	250 μm
Mass flow rate (Q)	59.5 g/min
Extrusion velocity (v_e)	24.1 m/min
Extrusion temperature (T)	260°C
Take-up velocity (v_W)	1000/1500/2000/2500 m/min
DDR	41.5/62.3/83.0/103.8

vertically usually by at least one drawdown godet. Depending on the use of the filaments, a wide variety of drawing states inline can be realized before winding the filaments on bobbins. The solid-state drawing of the fibers is conducted between two godets, whereas the consecutive godet revolves faster than the first one. In this study, the spinning was realized with no inline drawing but with an offline solid-state drawing step. Take-up velocity v_W is varied between 1000 and 2500 m/min for the examination of the melt spinning process. The drawdown ratio is calculated as the ratio between take-up and extrusion velocity:

$$\text{drawdown ratio} = \frac{v_W}{v_e}$$

The spinning parameters are summarized in Table II. The fibers spun at the highest take-up velocity are used for further processing. These multifilaments have $n = 34$ filaments and a total titer of 239 dtex, which corresponds to a single-filament fineness of 7 dpf. With the help of the approximate density of the material,[25] the filament diameter of 22 μm is calculated.

Draw winding

Draw winding is used for a continuous drawing of the fibers by godets rotating at different velocities, which define the draw ratio. The machine consists of three drawing zones (four godets), where the last three godets can be heated. The last drawing zone is equipped with a heating plate to control more exactly the drawing temperature. Previous studies at Institut für Textiltechnik der RWTH Aachen (ITA) have dealt with the calculation of the resulting fiber temperature for multifilament yarns, which can be significantly lower.[26]

For a detailed evaluation of the influence of the drawing temperature, the first two drawing zones remain constant with low drawing ratios of 1.05 and 1.08. Godet temperatures are set to 80°C for preheating the fiber. The main influence on the structure is then caused by the third drawing zone, for which the temperature can be controlled with the heating plate. For this zone, drawing ratios and

TABLE III
Parameters for Draw Winding

Parameter	Value
Draw ratio (zone 1)	1.05
Draw ratio (zone 2)	1.08
Draw ratio (zone 3)	1.0/1.1/1.2/1.25/1.3/1.35/1.4/ 1.5/1.6
Ratio (godet 4/winder)	0.93
Temperature (godet 1)	Room temperature
Temperature (godet 2)	80°C
Temperature (godet 3)	80°C
Temperature (godet 4)	30°C
Temperature (heating plate)	40°C/60°C/80°C/100°C/120°C/ 130°C/140°C/150°C/160°C

temperatures are varied starting from a defined standard process with ratio 1.4 and plate temperature 140°C. After the last drawing zone, a relaxation of the fiber is realized with a ratio of 0.93 between the last godet and the winder, which operates at a take-up velocity of 300 m/min. The parameters for draw winding and variations are summarized in Table III. After the drawing process, the filament's diameter has decreased from 22 to 18 μm in the standard drawing process. The fineness is also reduced to about 160 dtex, which corresponds with 4.7 dtex per filament.

Characterization

WAXD was used to examine the crystal structure and preferred crystallite orientation of all produced and processed fibers. The experiments were carried out with a single-crystal diffractometer STOE IPDS II equipped with an image plate for digital readout and two independent goniometer circles. The diffractometer uses a Mo-K_α X-ray tube, for which a voltage of 50 kV and a current of 25 mA were selected. The detector distance was chosen at 200 mm from the sample, allowing an 2θ angular range from 1.2° to 40°. The collimator width chosen was 500 μm. The exposure time of 3 min per sample gave a good signal-to-noise ratio.

A special specimen holder for fibers was constructed for a parallel alignment of the material for experiments at room temperature, allowing reproducible results and the examination of the orientation distribution of crystals of the different phases. The exact position of the fiber sample in the X-ray beam is controlled by a digital camera positioned in the diffractometer.

For measurements at elevated temperatures, the diffractometer was equipped with a furnace for heating the sample with a hot air stream. The temperature of the furnace T_F was measured by a built-in thermocouple and controlled by a proportional-inte-

gral-derivative controller (PID controller). The temperature range was chosen between room temperature and 250°C with a constant heating rate of 0.2°C/ min. With 3 min of exposure and 2 min for readout, the diffraction pattern could be recorded every 1°C. The exact temperature at the sample position T_s was controlled and calibrated by a thermocouple placed on a common goniometer head. The temperature dependence between sample and furnace is linear so that the sample temperature can be calculated:

$$T_s = aT_F + b, \text{ with } a = 0.780 \pm 0.001 \text{ and}$$
$$b = 10.21 \pm 0.18°C$$

The fibers were placed in glass capillaries of 500 μm diameter, allowing the melting of samples in the diffractometer.

The first goniometer circle, allowing rotations about the fibers axis, could be chosen arbitrarily because of the rotation symmetry of the sample. The second goniometer circle was used to tilt the fiber from a perpendicular incident of the radiation. A continuous rotation between 10° and 25° was chosen for recording the diffraction intensity of the (002) plane in the α phase and the (001) plane in the β phase. The angles were determined by the consideration of the reciprocal space. For satisfying the condition for constructive interference, the sample must be tilted by the same angle as the diffraction angle 2θ. This can be realized by the indicated rotation. The integration width is chosen because of the orientation distribution in the fibers, causing the X-ray beam to be scattered to angles around the initial exact position.

Intensity distribution from air scattering and signal noise was recorded in the same configuration, but with an empty specimen holder, and subtracted from the measured data. A special software tool for processing the image plate data was developed at ITA. The software is capable of calculating intensity profiles in both directions 2θ and the azimuthal angle φ for arbitrary ranges in φ and 2θ, respectively, with a definable integration range. The tool was used for determining the profiles from the regions shown in Figure 1.

The first region in Figure 1(a) allows the examination of the lattice planes with $l = 0$ (hk0) from the crystal phases and the intensity distributions of the noncrystalline parts of the material. The full angular range in φ is chosen because of the almost uniform intensity profile of this phase in azimuthal direction, allowing the quantitative evaluation of the calculated profiles. The second scan in Figure 1(b) is used to obtain information about the lattice planes indicated with (00l), which contain information about the regular conformations in the polymer. The third scan in Figure 1(c) is carried out along the direction φ,
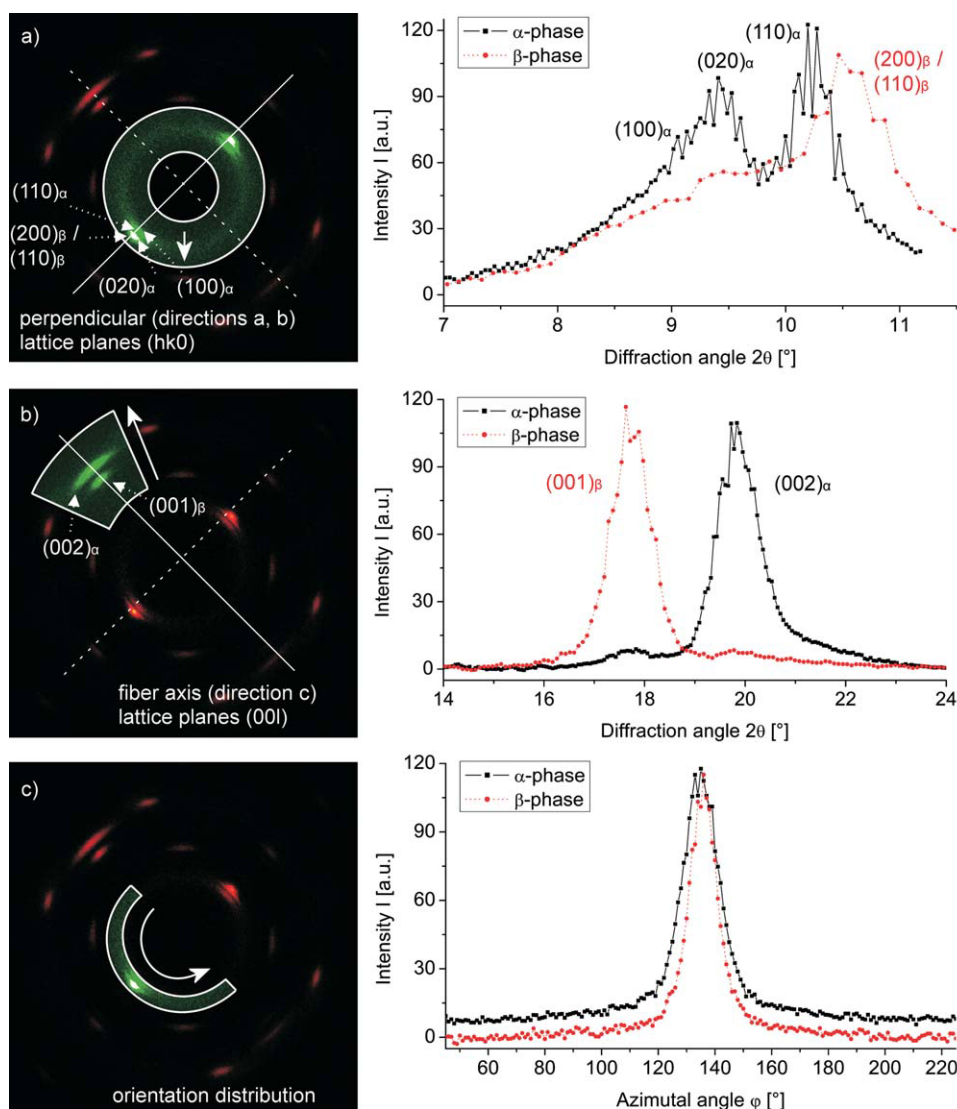
Figure 1 Regions for calculating the intensity profiles (left) and resulting profiles for α and β fibers (right): (a) intermolecular distance for crystalline and noncrystalline regions; (b) intramolecular distance for crystal phases; (c) orientation distribution of crystalline and noncrystalline regions. [Color figure can be viewed in the online issue, which is available at wileyonlinelibrary.com.]

allowing the evaluation of the orientation of all present phases.

Further evaluation of the integrated profiles and peak fitting is done with the OriginPro software from Origin Lab (Northampton, MA).[27] Uncertainties of the fitted values are calculated from the covariance matrix. Since intensity values are determined by a counting process with a number of counts N, the errors of these values should be counted by $\sqrt{N}$. Furthermore, the limited resolution of the image plate system must be taken into account. This effect should not be considered as an error on the image plate position and rather contributes to the width of intensity distributions in both directions 2θ and φ. Therefore, the resulting peak profiles (width w_0) must be seen as a convolution of two distributions coming from the sample (width

w_s) and from the image plate (width w_{IP}). The contributions from the image plate are examined at different positions 2θ by a silicon powder with large crystallites and subtracted from the measured values:

$$w_s = \sqrt{w_0^2 - w_{IP}^2}$$

Conventional and temperature-modulated DSC is used to compare the degree of crystallinity and determine the enthalpies of the observed phase transitions. The experiments were carried out with a Mettler Toledo DSC 1 equipped with a FRS5 sensor having 56 thermocouples. The fiber samples were cut into pieces of 2–3 mm length with a total weight of about 5 mg, placed into 20-μL aluminum crucibles, and pressed to the bottom of the crucible with

a lid for a good heat contact. The crucibles were placed on the sensor with an automatic sample changer, allowing reproducible results. N_2 was used for purging the furnace to reduce the formation of ice at temperatures below 0°C. Conventional DSC was carried out with heating rates of 2, 5, and 10°C/min in the temperature range from −90 to 250°C.

For the temperature-modulated DSC, the special TOPEM® (Mettler Toledo brand name) technique developed by Mettler Toledo was used. The constant heating ramp of 2°C was modulated with heat pulses of 0.5°C and a stochastically varied length. This method allows the frequency-independent separation of reversing and nonreversing components of the heat flow by analyzing the impulse response of the sample.[28] DSC thermograms are evaluated with the Mettler Toledo STARe software with the capability of calculating the specific enthalpies and peak temperatures.

DMA was carried out with a Mettler Toledo DMA/SDTA861e. The fiber with a length of 9 mm was clamped into a specimen holder for applying uniaxial stress. The experiments were carried out with a maximum force of 0.2 N and a maximum dynamic displacement of 40 μm. A constant static displacement of about 70 μm was applied for measuring the tension in the elongation and the contraction phase of the period. The experiments were carried out with a harmonic displacement at frequencies of 1 and 10 Hz with a heating rate of 5°C/min in a temperature range from −120 to 200°C. The mechanical response of the sample was recorded phase sensitive, allowing the calculation of the storage modulus E' and the phase shift $\tan(\delta)$ between applied force and detected displacement.

RESULTS

Wide-angle X-ray diffraction

Intensity profiles from the first region in Figure 1 contain the intensity peaks of the (110), (200), and (010) lattice planes from the α phase, the combined (110)/(200) peak from the β phase as well as the broad intensity distribution from the noncrystalline phase. For each crystalline peak, a pseudo-Voigt peak, with the intensity distribution

$$I(x) = (1 - \eta) \frac{A}{\sqrt{2\pi}w} \exp\left(-\frac{1}{2}\frac{(x - x_c)^2}{w^2}\right) + \eta \frac{1}{\pi} \frac{A \cdot w}{w^2 + (x - x_c)^2}$$

is fitted. Pseudo-Voigt peaks are used to describe distributions with both Gaussian and Lorentzian parts. The parameter μ = 0.6, which specifies the Lorentzian fraction, is fixed for a better comparison

of the values determined for different fibers. The noncrystalline intensity is described with a Gaussian distribution:

$$I(x) = \frac{A}{\sqrt{2\pi}w} \exp\left(-\frac{1}{2}\frac{(x - x_c)^2}{w^2}\right)$$

The center parameter x_c allows the calculation of the lattice parameters a and b of the α phase with the help of the Bragg equation, where d is the spacing between the lattice planes:

$$n\lambda = 2d \sin\theta$$

For all fibers, the calculated values are about 0.02 Å smaller than for samples from quiescent, mechanical stress–free crystallization for the perpendicular direction. The sample used for comparison was slowly cooled from the melt and examined with the same configuration. For the β phase, no lattice parameters a and b can be calculated because of the overlapping intensity distributions. The center value from the noncrystalline peak is considered as the mean distance between the polymer chains being calculated with the Bragg equation.

The half-width parameter w is linked to the crystallite size d by the Scherrer formula:

$$d_{a,b,c} = \frac{\lambda}{w_{a,b,c} \cos\theta_{a,b,c}}$$

Since no function for the crystallite size distribution is known, only the mean value of the crystal size can be calculated to compare dimensions in the directions of different lattice planes d_a, d_b, and d_c as well as between different fibers. Also, the width from the noncrystalline regions is interpreted as the coherence length of short-range order between the polymer chains.

The areas A of the peaks are used to calculate the total mass of crystalline regions in the sample. The scattered intensity is proportional to the square of electron density. Furthermore, the selected region of the diffraction pattern in Figure 1(a) is representative because it only contains intensity contributions from lattice planes, whose normal is perpendicular to the fiber axis. These lattice planes contain the same amount and types of atoms in the two crystalline phases α and β, as well as the noncrystalline one, so that the crystallinity may be computed with the following formula:

$$X_c = \frac{A_\alpha + A_\beta}{A_{total}}$$

The second region in Figure 1(b) is evaluated by a peak fit of two pseudo-Voigt peaks, revealing information about the lattice constant c in both crystal phases. Here, the d-spacings are larger than for

Comparison of Crystal Parameters in Fibers and from Quiescent Crystallization for the α Phase

Parameter	α Phase (quiescent)	α Phase (fiber)	β Phase (fiber)
Lattice parameter a (Å)	4.96 ± 0.01	4.95 ± 0.01	–
Lattice parameter b (Å)	9.64 ± 0.02	9.59 ± 0.01	–
Lattice parameter c (Å)	4.62 ± 0.01	4.64 ± 0.01	2.57 ± 0.01
Crystallinity (%)	37.2 ± 1.1	23.0 ± 1.3	26.9 ± 1.4
Crystallite dimension d_a (Å)	85.6 ± 1.8	90.7 ± 1.0	–
Crystallite dimension d_b (Å)	118.0 ± 2.5	131.7 ± 4.3	–
Crystallite dimension d_c (Å)	55.7 ± 0.5	56.7 ± 0.4	65.1 ± 0.2
Orientation f crystal phase	0.0	0.991 ± 0.004	0.993 ± 0.002
Chain distance mesophase (Å)	4.85 ± 0.04	4.74 ± 0.05	4.66 ± 0.02
Distance short-range order (Å)	14.3 ± 0.3	18.7 ± 0.2	22.2 ± 0.1
Orientation f mesophase	0.0	0.42 ± 0.01	0.46 ± 0.01

quiescent crystallization. All parameters together indicate uniaxial mechanical stress applied in the *c* direction of the unit cell, leading to a specific deformation of the crystal structure. In this case, positive stress occurs along the *c* direction and leads to an elongation. Negative stress occurs along the *a* and *b* directions, resulting in a transverse contraction. The half-width parameter of both phases is quite larger than that for the other lattice planes, indicating platelet-like crystal morphology in the fibers.

The peak areas can be used for deriving the relative amount of α and β phase in the sample. The correlation has been proven with an experiment, where a variable number of fibers containing pure α and β phase with known textile titer (mass per length) were mixed to give "reference samples" with known mass fractions of both crystalline phases. With this method, seven samples were created with different amounts of crystalline phases. The relative peak area

$$A_{\text{rel}} = \frac{A_\beta}{A_\alpha + A_\beta}$$

is plotted against the mass fraction of the β phase with a following linear regression. The χ^2 of 1.1 indicates the exact correlation between the two parameters.

For the orientation distribution deduced from Figure 1(c), a Gaussian intensity profile is assumed for the crystalline phases having well-resolved peaks. For the noncrystalline regions, a second Gaussian profile and a constant intensity offset are chosen. The total area of the profile and the offset are assumed to be caused by the noncrystalline regions and must be considered when calculating the orientation factor. The calculated profiles I_{calc} are used for the calculation of the standard deviation of the azimuthal angle $\langle \sin^2 \varphi \rangle$:

$$\langle \sin^2 \varphi \rangle = \frac{\int_0^{2\pi} \sin^2 \varphi \, I_{\text{calc}}(\varphi) \, d\varphi}{\int_0^{2\pi} I_{\text{calc}}(\varphi) \, d\varphi}$$

The obtained values can be used to calculate the orientation factor for crystalline and noncrystalline phases:

$$f = 1 - \frac{3}{2} \langle \sin^2 \varphi \rangle$$

The calculated values show that the crystals of both crystalline phases α and β are nearly perfectly oriented along the fiber axis. But even the noncrystalline regions show a clear preferred orientation along the axis, which is deduced from the nonuniform intensity distribution on the ring in the diffraction patterns. Furthermore, the coherence length over four to five polymer chains is considerably larger than the expected one to the nearest neighbor in an amorphous polymer. These two observations lead to the conclusion, that the noncrystalline regions should be considered as an oriented mesophase. Such a phase is not uncommon for some polymers.[29]

All evaluations described in this part are summarized in Table IV for a representative α and β fiber and compared with values known from quiescent crystallization.

The temperature-dependent experiments allow the calculation of anisotropic thermal expansion coefficient in *a*, *b*, and *c* direction for the α phase and in *c* direction for the β phase. Furthermore, the change in the mean distance between noncrystalline polymer chains can be evaluated. The values for thermal expansion are calculated by a linear regression, whereas the uncertainties are determined by the propagation of uncertainty of the calculated lattice constants.

In the *c* direction of both crystalline phases, the negative values for α_c indicate an anomalous thermal expansion, which even increases for temperatures higher than 130°C. In Figure 2, the evolution of the lattice parameters and the calculated values for the thermal expansion are displayed.

Furthermore, the positive expansion coefficient for the mesophase extends to a value five times larger at this temperature as shown in Figure 3. Together with the decreasing orientation factor of this phase, as shown in Figure 4, the indicated temperature can be understood as a softening point of the mesophase. This softening is assumed to allow a
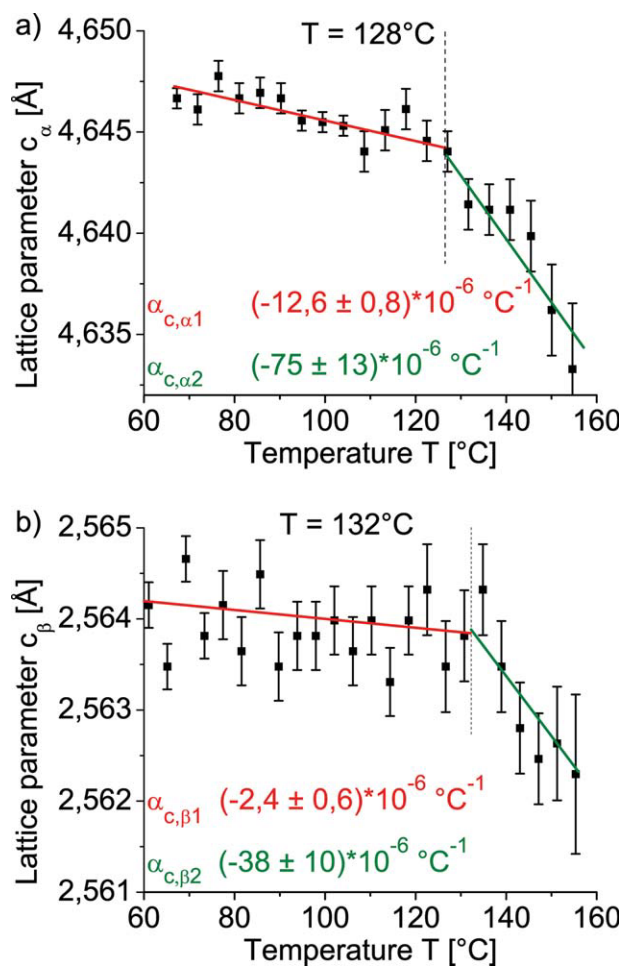
a)

b)

Figure 2 Determination of anisotropic thermal expansion coefficients in *c* direction for the α phase (a) and the β phase (b). (c) orientation distribution of crystalline and noncrystalline regions. [Color figure can be viewed in the online issue, which is available at wileyonlinelibrary.com.]

mechanical relaxation of the crystal phases and the resulting decrease of the lattice parameters.

At temperatures higher than 160°C, the $(001)_\beta$ reflection of fibers containing the β phase disappears in combination with the appearance of the $(002)_\alpha$ reflection, indicating a phase transition from β to α phase (see Fig. 5). For higher temperatures, all fibers contain the α phase.

For temperatures higher than 168°C, a significant change in the orientation distribution occurs, as shown in the diffraction pattern and the azimuthal reflection position of the $(002)_\alpha$ lattice plane in Figure 6.

This change is accompanied by a massive change in thermal expansion of the $(010)_\alpha$ lattice plane changing from normal [$\alpha = (96 \pm 11) \times 10^{-6}°C^{-1}$] to anomalous expansion [$\alpha = (-345 \pm 46) \times 10^{-6}°C^{-1}$]. For a temperature of 172°C, these changes reach their maximum value. The new lattice parameters, $a = 4.97$ Å, $b = 9.67$ Å, and $c = 9.24$ Å, correspond to the values known for the γ phase.[8] In this step, the absolute intensity and therefore the crystallinity
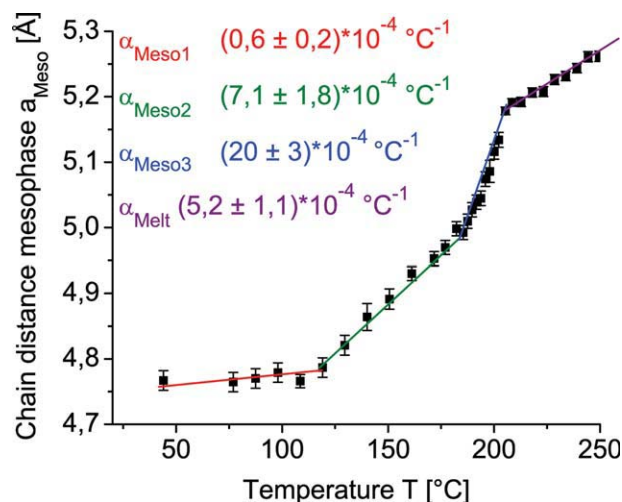
Figure 3 Thermal expansion of the mesophase perpendicular to the polymer chains, with the anisotropic thermal expansion coefficients indicated. [Color figure can be viewed in the online issue, which is available at wileyonlinelibrary.com.]

decrease so that parts of the α-phase crystallites are not converted to the γ phase, but to a noncrystalline state.

Together with this massive change, another variation of the thermal expansion of the mesophase occurs with an extremely large value $\alpha = (20 \pm 3) \times 10^{-4}°C^{-1}$ (see Fig. 3).

For temperatures higher than 187°C, the Bragg reflections disappear in the recorded images, together with a change of thermal expansion of the mesophase [$\alpha = (5.2 \pm 1.1) \times 10^{-4}°C^{-1}$]. These events are considered as the final melting of the sample.

Differential scanning calorimetry

Conventional DSC thermograms of fibers containing pure α and pure β phase are displayed in Figure 7
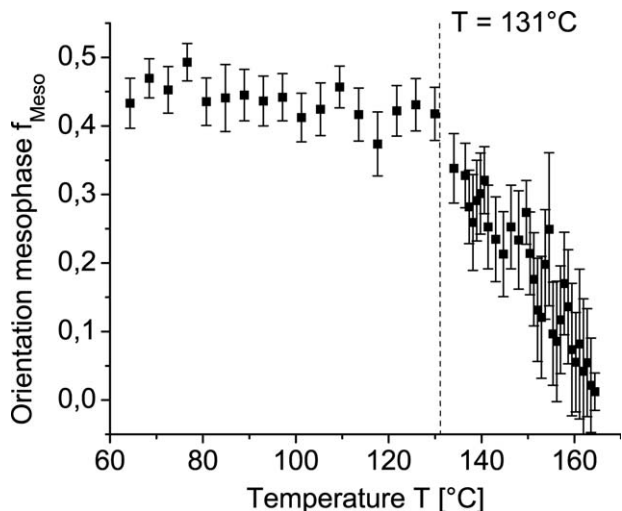

Figure 4 Temperature-dependent decrease of the mesophase orientation factor.
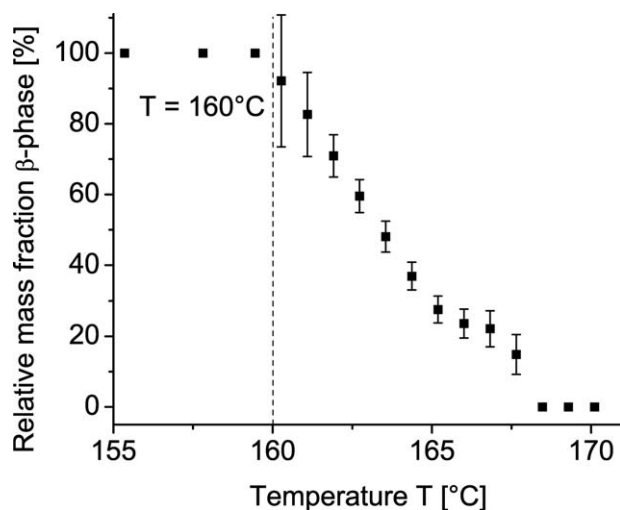
Figure 5 Changes in the relative intensity of α and β phase indicating the β to α transformation.

for the first heating, compared with a slowly cooled sample in the DSC for a heating rate of 10°C/min.

There is no signature of the glass transition in any of the samples between −40 and −35°C, where this transition is expected.[8] Consequently, the change in heat capacity is vanishingly small and is not detectable. A small endothermic signal can be observed at temperatures around 50–60°C in all samples, which is the temperature for a mechanical relaxation described in the next section.

During melting (temperature range from 160 to 190°C), several overlapping peaks show up. The first peak of the fiber containing the β phase is around 160°C, whereas the first peak of the samples contain-
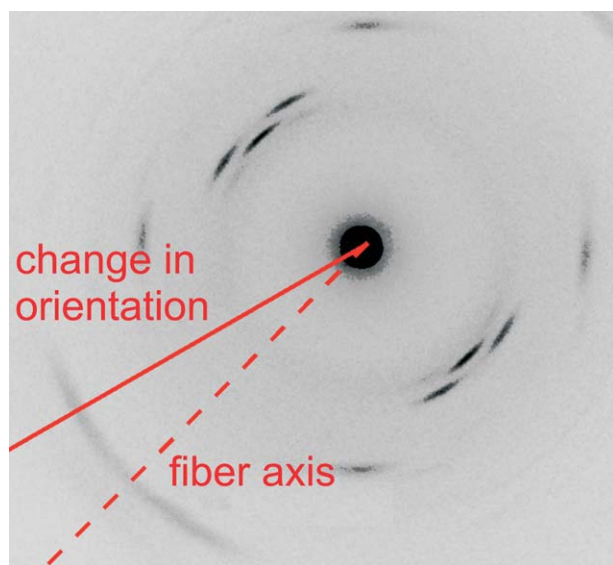

Figure 6 Diffraction pattern of the γ phase with modification of orientation distribution. [Color figure can be viewed in the online issue, which is available at wileyonlinelibrary.com.]
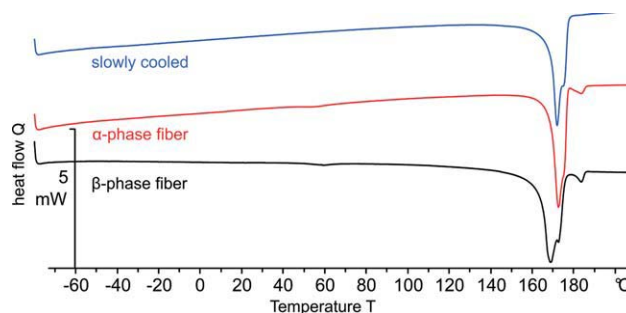

Figure 7 DSC thermograms of a slowly cooled sample and fibers with α and β phase. [Color figure can be viewed in the online issue, which is available at wileyonlinelibrary.com.]

ing the α phase occurs at around 170°C. Consequently, the first peak must be considered as a phase transition or the melting of the β phase. The last peak only occurs in the fiber samples and at temperatures around 185°C and vanishes in the slowly cooled sample.

Total melting enthalpy ΔH is calculated from the area of all melting peaks. Normalizing this value with the melting enthalpy of a 100% crystalline sample ($\Delta H_0 = 104.7$ J/g) delivers the crystallinity X_c^{DSC} of the sample:

$$X_c^{DSC} = \frac{\Delta H}{\Delta H_0}$$

For all fibers, X_c^{DSC} is about 70–80% and much higher than the values derived from X-ray diffraction. The measured binding energy mainly depends on the interaction with the nearest neighbor molecule, which can be evaluated by treating the dipole–dipole interaction of two molecules at a typical distance of $r = 4.7$ Å (U_1) and the next neighbor at $2r = 9.4$ Å (U_2):

$$U_1 = \frac{2p^2}{4\pi\varepsilon_0 r^3} \approx 0.10 \text{ eV} \quad \text{and}$$

$$U_2 = \frac{2p^2}{4\pi\varepsilon_0 (2r)^3} \approx 0.01 \text{ eV}$$

The mesophase is also characterized as an ordered state with well-oriented molecules. Therefore, enthalpy contributions at the transition to the very much less ordered melt can be expected. Since orientation and order are less pronounced than in the crystal phases, the contributions to the total enthalpy of melting must be lower than the values known for pure crystalline material. The total enthalpy

$$\Delta H = \Delta H_{\alpha\beta} + \Delta H_{meso}$$

can only be considered as an averaged amount for total binding energy of all phases. The two methods, DSC and WAXD, measure different kinds of
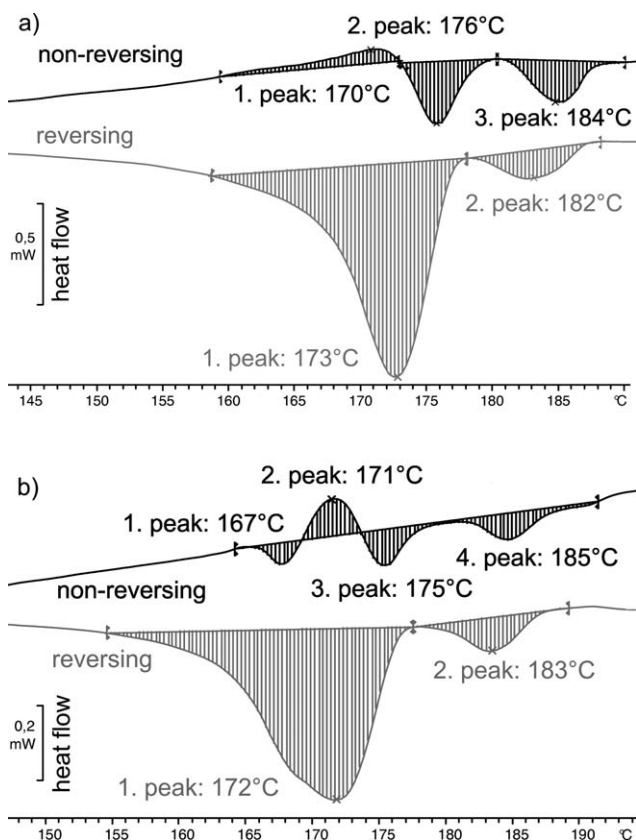
Figure 8 Reversing, nonreversing, and total heat flow of fibers consisting of pure α (a) and pure β (b) phase.

crystallinity, whereas the information from X-ray diffraction can be taken as the crystallinity defined by the long-range order of the crystal state. This information is important in the case of functional polymers, where the special function depends on one specific crystal phase. However, many properties such as the mechanical strength depend on the total binding forces. In this case, the value deduced from thermal analysis should be taken into account.

For a further study of the overlapping distributions, the TOPEM technique is considered. The resulting thermograms are shown in Figure 8 for a fiber containing pure α [Fig. 8(a)] and one containing pure β [Fig. 8(b)] phase.

The separation of the total heat flow into the reversing and nonreversing heat flow depends on the heating rate and the amplitude of heat pulses. This causes components of the nonreversing heat flow to appear as a reversing process or *vice versa* so that the calculated enthalpies can only be considered qualitatively. However, the procedure gives an accurate temperature signal to determine the transition temperatures.

Since the crystal structures in PVDF fibers are formed far from equilibrium, in a stress field and with a distinguished orientation, the heat pulses lead to the melting of the crystallites in the heating

phase and a recrystallization in the cooling phase. The resulting crystal structure is the thermodynamically stable one at the corresponding temperature. Therefore, structural phase transitions are possible. Their signal is expected mainly in the nonreversing part of the heat flow. In the case of higher binding forces in the new phase, the heat flow peak due to this transition is exothermic, whereas for lower binding an endothermic process is expected. If the same crystal phase reappears, a contribution to the reversing heat flow can be expected. There are three transitions in the α phase fiber (exothermic at $170 \pm 2°C$, endothermic at $175 \pm 2°C$, and endothermic at $184 \pm 2°C$), extended by a fourth transition (endothermic) in the β phase at $164 \pm 2°C$.

For the correlation of the heat flow peaks with the present phases, the mesophase has to be taken into account. Because this phase is much closer to the equilibrium, the corresponding signal is estimated in the reversing heat flow. Since crystallites remain in the fiber, the mesophase melts in the heating phase and appears in the same form during cooling. The reversing heat flow indicates two separate endothermic processes at 173 ± 5 and $182 \pm 5°C$. This interpretation of the data is in good agreement with the transitions observed in the diffraction pattern for the mesophase, since the number and temperatures of observed events are consistent.

Dynamic mechanical analysis

The mechanical response is examined exemplarily for one fiber with pure α phase, one with pure β phase, and one with mixed phases. The results for the storage modulus E' and the phase shift $tan(δ)$ are displayed in Figure 9.

By DMA, the glass transition of PVDF fibers can easily be measured. We find it at $-40°C$ [peak in $tan(δ)$] and $-35°C$ for the α-phase- and the β-phase-containing fiber, respectively. The phase-dependent peak shifts indicates that the mobility of the polymer chains is reached at higher temperatures, which could be caused by the larger degree of crystallinity and higher binding forces in the noncrystalline regions.

A further change in the mechanical response can be observed at temperatures around $50°C$. Upon heating, the modulus of the α fiber decreases considerably, and $tan(δ)$ increases. This frequency-independent change is considered as a relaxation process known from other polymers as the $α_c$ relaxation. This process does not occur in the β-phase fiber and is much weaker in the fiber containing both phases, and so it is assumed to take place in the α phase. In contrast to this weakening process, the modulus of fibers containing the β phase is enhanced in the same temperature range. This could be explained by the formation of new crystalline regions or a higher
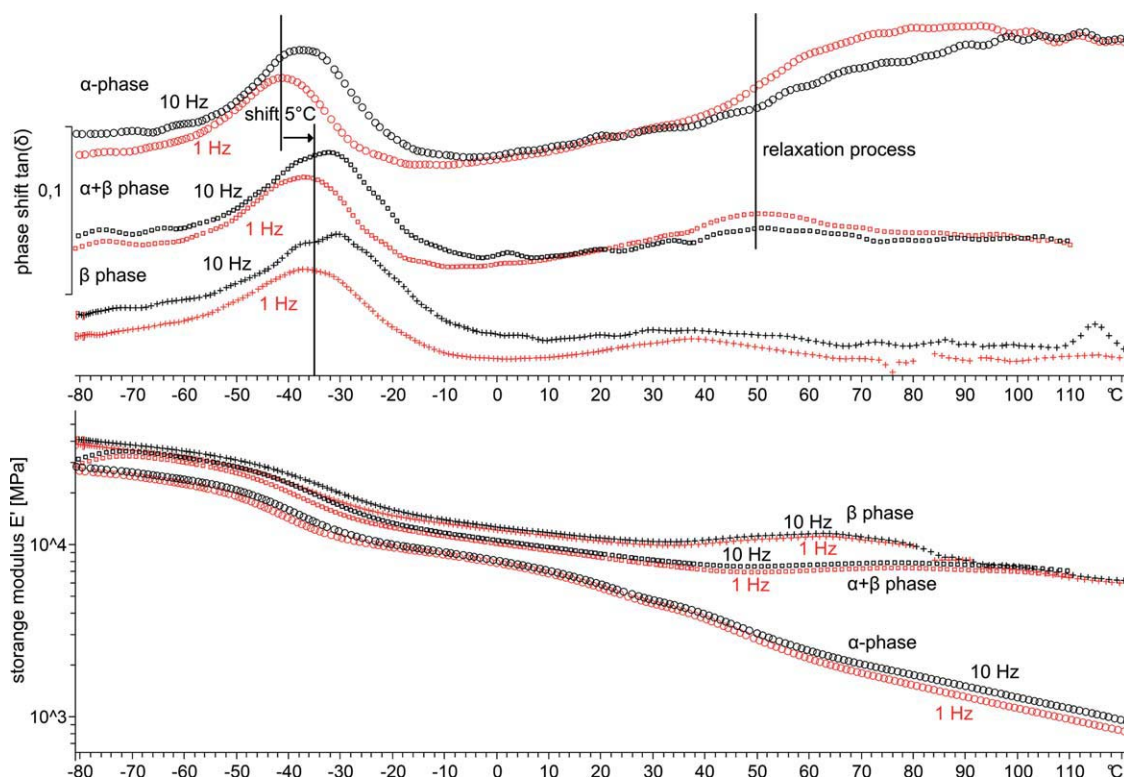
Figure 9 Dynamic mechanic response [phase shift tan(δ) (a) and total modulus E (b)] of α, β, and mixed phases fiber. [Color figure can be viewed in the online issue, which is available at wileyonlinelibrary.com.]

orientation in the noncrystalline regions, where therefore entropy elasticity is reduced. Another softening event of the fiber is suspected at temperatures higher than 130°C, which cannot be measured with the chosen parameters.

DISCUSSION

Melt spinning and draw winding

Melt spinning at different take-up velocities mainly affects the orientation of the α phase and the mesophase in the fibers (see Fig. 10), whereas the total crystallinity (defined by WAXD) varies only slightly. For the highest take-up velocity of 2500 m/min, a maximum mass fraction of 0.6% β-phase crystals is formed.

DSC thermograms show a larger peak at 185°C for higher take-up velocities, which was identified as the melting of the γ phase in the temperature-dependent WAXD experiments. This indicates a larger amount of this phase with increasing mechanical stress and orientation, explaining the absence of this transition in slowly crystallized material.

The variation of the draw ratio in the draw winding process increases the amount of the β phase. For draw ratios less than 1.5, the total crystallinity remains constant, indicating an α to β transition. In general, fibers containing larger amounts of β phase with the same total crystallinity show a larger total enthalpy in DSC,

which can be caused by a higher melting enthalpy of this crystal form or the higher degree of orientation of the mesophase in these samples. For higher draw ratios, overall crystallinity increases during the drawing process, which must be caused by growth or formation of new β crystallites from the mesophase. A total α to β conversion and a maximum total mass fraction of 27.8 $\pm$ 0.7% is achieved only at the highest drawing ratios close to the fracture of the filaments.
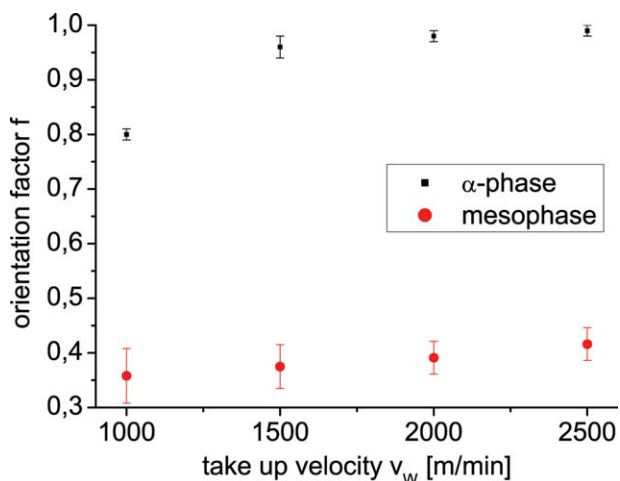

Figure 10 Dependency of the orientation factors for α phase and mesophase on the take-up velocity. [Color figure can be viewed in the online issue, which is available at wileyonlinelibrary.com.]
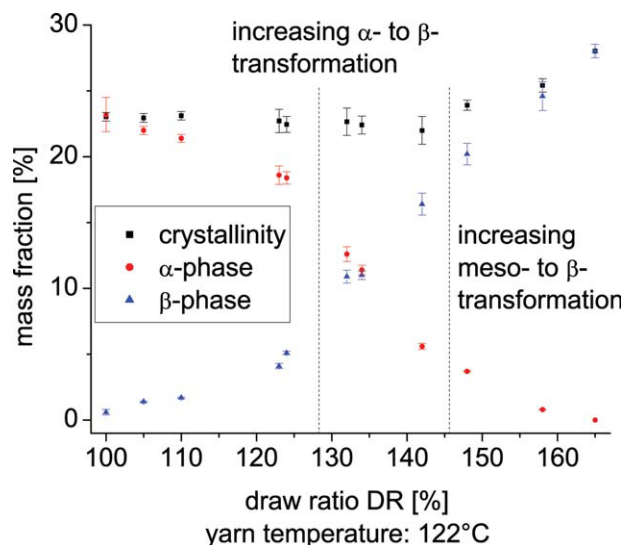
Figure 11 Phase contents at different draw ratios in the draw winding process, with the corresponding transitions in the material indicated. [Color figure can be viewed in the online issue, which is available at wileyonlinelibrary.com.]

The resulting phase contents and the corresponding transitions are displayed in Figure 11.

For the discussion of the effect of drawing temperature, the lower yarn temperature must be considered.[25] The following results are displayed with the corrected temperature assumed for the PVDF fibers, which is about 20°C lower than the temperature of the heating plate. The development of phase contents is shown in Figure 12.

There are two steps in the total mass fraction of the β phase, which are caused by a larger transformation rate from the α phase (>50°C) and the mesophase (>130°C). These phenomena are later discussed as relaxation processes in correlation with the DMA experiments.

Melting

Structural phase transitions during the melting of fibrous PVDF are derived from the diffraction patterns at higher temperatures, showing the changes in the crystal geometry and orientation, together with the temperature-modulated DSC, allowing the detection of the related thermodynamic quantities qualitatively. The uncertainties on the temperature values are derived from the averaging of the temperatures determined for different fibers.

The first transition occurring during the melting process is the transforming of β-phase crystallites to the α-phase crystallites starting at a temperature of 164 ± 2°C. This process can be clearly identified in the diffraction patterns by comparing the relative intensity of the $(001)_\beta$ and $(002)_\alpha$ reflections. From the nonreversing heat flow thermogram (see Fig. 8), the

whole transition can be identified as an endothermic process.

The second transition, common to all fibers, is the conversion of the α phase to the γ phase at 170 ± 2°C. The angle $\beta = 92.7°$ for the monoclinic γ unit cell of this phase is much smaller than the observed change in the orientation distribution. In the case of an unchanged orientation distribution of the crystallites, the reflections should only shift by 2.7°, which is the difference between the β angles. However, the observed value of $\Delta\varphi = 19.1°$ can be associated with the conformation change from TGTG′ to TTTGTTTG′. Since the new γ conformation has more trans-sections, its length increases to 9.74 Å. When this polymer chain is placed in the unit cell with $c = 9.24$ Å, it cannot be oriented along the c axis. The angle between the axis and the carbon backbone then corresponds to the angular change in the diffraction patterns:

$$\Delta\varphi = \arccos\left(\frac{9.24\ \text{Å}}{9.74\ \text{Å}}\right) \approx 18.4°$$

The new orientation distribution function is then caused by new directions a and c of the γ phase, which are not perpendicular and parallel to the fiber axis, respectively. Since the angles α and γ of the unit cell remain right angled, the crystal axis b stays perpendicular to the fiber axis. However, there are two possible directions of the new unit cell in the fiber, which are statistically occupied. This phenomenon causes the appearance of one reflection at two azimuthal positions and is known as the twinning in common single crystals. The underlying
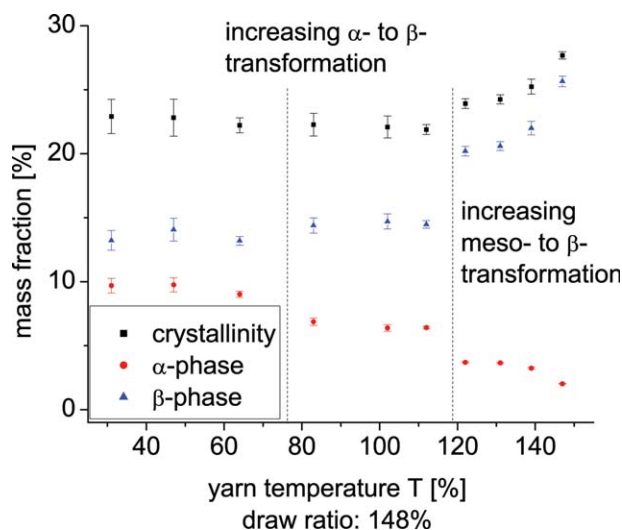

Figure 12 Phase contents at different yarn temperatures (calculated from heating plate temperature), with the corresponding transitions indicated. [Color figure can be viewed in the online issue, which is available at wileyonlinelibrary.com.]

TABLE V
Structural Phase Transitions During Melting of PVDF Fibers

Transition	Temperature (°C)	Process	X-ray data
$\beta \rightarrow \alpha$	164 ± 2	Endothermic	Relative intensity changing from 002_α to 001_β
$\alpha \rightarrow \gamma$	170 ± 2	Exothermic	Change in orientation distribution
$\alpha \rightarrow$ Melt	175 ± 2	Endothermic	Decreasing absolute intensity
$\gamma \rightarrow$ Melt	184 ± 2	Endothermic	Disappearing reflections
Mesophase $\rightarrow$ transformed mesophase	173 ± 5	Endothermic	Thermal expansion increased
Transformed mesophase $\rightarrow$ melt	182 ± 3	Endothermic	Thermal expansion reduced

conformation change cannot be described by a discrete flip of every second gauche- to trans-conformation, since this mechanism would produce either gauche or antigauche bonds. Instead, a continuous transformation is expected and confirmed by the experimental data, since the change in the orientation distribution from $\Delta\varphi = 0°$ to $\Delta\varphi = 19.1°$ is also detected as a continuous process, where the reflection position moves away from the fiber axis with increasing temperature.

The nonreversing heat flow chart (Fig. 11) shows the exothermic nature of the transformation. Because absolute reflection intensities decrease during the transformation, this process is also accompanied by a partial transition to a noncrystalline or liquid state. This endothermic transformation of the α phase can also be found in the TOPEM thermograms at 175 ± 2°C.

The last transformation of the crystalline parts of the material, also occurring in all fibers, is the final melting of the material starting at 185 ± 2°C, which is an endothermic process. This process is derived from the decreasing reflection intensities until the diffraction pattern is reduced to the diffuse scattering of the noncrystalline or liquid polymer.

The mesophase shows a similar transformation as the α phase, starting at a temperature of 173 ± 5°C. Since long-range order is much less pronounced than in the crystalline phase, the transformation can only be observed in the massive change of thermal expansion in the noncrystalline regions. As described in "Experimental," the resulting enthalpy is expected in the reversing heat flow chart, which shows a peak over a broad temperature range. Melting of the transformed mesophase occurs at temperatures higher than 182 ± 3°C. The transition is identified by another change in the thermal expansion coefficient and a second heat contribution in the reversing heat flow chart.

All transitions observed and analyzed during the melting of the fibers are summarized in Table V. Since all events can be derived from temperature-modulated DSC, where temperature measurement is much more exact and reproducible than in the WAXD case, the temperature values and the uncertainties are taken from the resulting thermograms.

Relaxation processes

Effects of relaxation processes can be observed in all experiments. The first process, occurring at temperatures higher than 50°C, can be clearly identified by the mechanic response measured in DMA experiments. As seen from the analysis of draw winding, this process causes a softening of the α-phase crystallites and allows the transformation to extended chain conformation of the β phase. Because chain conformation in fibers containing β-phase crystallites is already extended, the mechanical response does not change in this case. The increase in Young's modulus in these fibers is assumed as an reorientation process in the noncrystalline regions resulting in a higher orientation of the polymer chains. The relaxation process also affects the thermal response of the fibers, as seen from the corresponding endothermic process in the thermograms. Since this process takes place in all fibers, the relaxation must be interpreted as a general softening. This softening event affects the torsion angles, which are weakened cooperatively in the crystal phases.

The second relaxation process concerns the mesophase and allows the transformation (or crystallization) to the β phase. Because of too weak mechanical response, this process can only be revealed from X-ray diffraction and the analysis of the fibers drawn at higher temperatures. Adjacent to the β formation, the process causes a higher thermal expansion and a decrease of orientation in the mesophase and a faster relaxation of the deformed crystalline unit cell to its equilibrium state. A temperature of 131°C is common to all these processes, which is interpreted as the relaxation temperature.

The effects of the two mechanical relaxation processes are summarized in Table VI. The uncertainties on the temperature values are derived from the averaging of the temperatures determined for the

TABLE VI
Relaxation Processes Observed in PVDF Fibers

Temperature (°C)	Transition (revealed from draw winding)	Effects
50 ± 3	α → β	tan(δ) increase in DMA; endothermic DSC peak
131 ± 2	Mesophase → β	Thermal expansion increase in mesophase; anomalous thermal expansion increase in crystal phases; orientation decrease in mesophase

different effects and the propagation of uncertainty on the temperatures measured in WAXD because all effects cannot be derived from the DSC thermograms.

Overview of phase transitions

Possible structural phase transitions in melt-spun PVDF fibers are summarized in Figure 13. The different arrows indicate the influence of the analyzed processes and the experiments which were carried out.

Melt spinning causes the formation of α phase and mesophase in the fibers, which differ in orientation and crystal geometry from the structures obtained from quiescent crystallization. Mechanical stress, occurring in draw winding and DMA experiments, causes the formation of the β phase, whereas it depends on the temperature if the transition takes only place in the α phase or also in the mesophase. In the first case, only a structural phase transition in the crystalline regions is allowed, whereas the second case results in a higher degree of crystallinity.

During the heating of the fibers with no external stress, several transformations occur, starting with the reconversion of β to α phase. The next transformation, the formation of the γ phase, is special for the internal mechanical stress appearing in fiber production and processing. A similar transformation to a high-temperature phase is expected in the mesophase as revealed from the change in thermal expansion.

CONCLUSION

In general, we achieved a detailed analysis of the crystal forms, phase contents, and structural phase transitions in PVDF fibers. The determination of crystallinity with WAXD and DSC showed great differences, which could be explained by taking into account the binding forces of nearest neighbor polymer chains in noncrystalline regions. In case of functional polymers like PVDF, where physical proper-

ties depend on specific crystalline polymorphs with long-range order, phase content can only be reliably derived from diffraction experiments. On the other hand, enthalpy of fusion measured by thermal analysis is a measure of different binding forces after the transition and all relating properties such as mechanical behavior.

Our study confirms the general fact that drawing is responsible for the β formation in PVDF fibers. However, we gained extended information about the mechanisms of mechanical relaxations involved in this transition and the corresponding temperature dependencies, allowing the optimization of the β crystallinity for the use in potential piezoelectric fibers. Since high drawing ratios lead to a higher mass fraction of the crystal phase, we suggest a low spinning speed causing higher elongation at fracture and higher possible draw ratios. First experiments with a take-up velocity of 1000 m/min and a draw ratio of 3.41 led to an increase of β crystallinity to a value of 34.8 ± 0.6%.

Additionally, the melting process of the polymer was analyzed in detail, where temperature-modulated DSC emerged as a good possibility for separating overlapping thermal events. In all fibers, the formation of the γ phase could be observed. A further characterization of the crystal morphology and orientation should be carried out, but requires new methods of structure refinement for two-dimensional diffraction patterns.

Furthermore, the study revealed the existence of an oriented mesophase. For the evaluation of the subjacent crystal morphology, further experiments involving small-angle scattering or imaging in real space have to be carried out. For a future
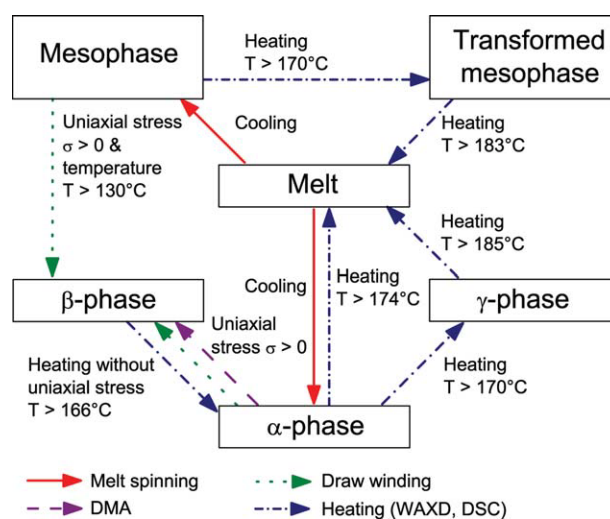

Figure 13 Possible structural phase transitions in fibrous PVDF, with the causative processing conditions and experiments indicated. [Color figure can be viewed in the online issue, which is available at wileyonlinelibrary.com.]

investigation of the polymer chain conformation and the detailed orientation of chemical bonds in this mesophase and the crystalline phases, FTIR spectroscopy could be carried out. Additionally, we are currently working on the examination of the crystallization mechanism and a kinetic model for describing crystallization and phase transitions in the material.

References

1. Lovinger, A. J. Science 1983, 220, 1115.
2. Ramer, N. J.; Stiso, K. A. Polymer 2005, 46, 10431.
3. Xu, J.; Johnson, M.; Wilkes, G. L. Polymer 2004, 45, 5327.
4. Ray, S.; Easteal, A. J.; Cooney, R. P.; Edmonds, N. R. Mater Chem Phys 2009, 113(2/3), 829.
5. Samon, J. M.; Schultz, J. M.; Hsiao, B. S.; Seifert, S.; Stribeck, N.; Gurke, I.; Saw, G. C. Macromolecules 1999, 32, 8121.
6. Houis, S.; Schedukat, N.; Gries, T. Chem Fibers Int 2007, 57, 122.
7. Laroche, G.; Marois, Y.; Guidoin, R.; King, M. W.; Martin, L.; Thien, H.; Douville, Y. J Biomed Mater Res 1995, 29, 1525.
8. Glen Kepler, R. In: Ferroelectric Polymers; Nalwa, H. S., Eds.; Marcel Dekker: New York, 1995; pp183–232.
9. Wang, T. T.; Herbert, J. M.; Glass, A. M. The Application of Ferroelectric Polymers; Blackie: Glasgow, 1988.
10. Herbert, J. M. Ferroelectric Transducers and Sensors. Gordon and Breach: New York, 1982.
11. Tashiro, K. In: Ferroelectric Polymers; Nalwa, H. S., Ed.; Marcel Dekker: New York, 1995; pp 63–182.
12. Takahashi, Y.; Masubara, Y.; Tadokoro, H. Macromolecules 1983, 16, 1588.
13. Nandi, A. K. Polymer 1994, 35, 5202.
14. Lund, A.; Hagström, B. J Appl Polym Sci 2010, 116, 2685.
15. Naegele, D.; Yoon, D. Y.; Broadhurst, M. G. Macromolecules 1978, 11, 1297.
16. Hasegawa, R.; Takahashi, Y.; Chatani, Y.; Tadokoro, H. Polym J 1972, 3, 600.
17. Tazaki, M.; Wada, R.; Ok Abe, M.; Homma, T. J Appl Polym Sci 1998, 65, 1517.
18. Davis, G. T.; McKinney, J. E.; Broadhurst, M. G.; Roth, S. C. J Appl Phys 1978, 49, 4998.
19. Sencadas, V.; Gregorio, R.; Lanceros-Méndez, S. J Macromol Sci Phys 2009, 48, 514.
20. Fourné, F. Synthetische Fasern, 1st ed.; Hanser: Munich, 1995. German.
21. Murata, A.; Ito, H.; Kikutani, T.; Okui, N. Seikei-Kakou 1998, 10, 554. Japanese.
22. Mhalgi, M. V.; Khakhar, D. V.; Misra, A. Polym Eng Sci 2007, 47, 1992.
23. Du, C. H.; Zhu, B. K.; Xu, Y. Y. J Appl Polym Sci 2007, 104, 2254.
24. Wulfhorst, B.; Gries, T.; Veit, D. Textile Technology, 1st ed.; Hanser: Munich, 2006.
25. Solvay Solexis. SOLEF 1006 PVDF Homopolymer. SOLVAY SOLEXIS S.A: Brussels, 2003. Available at www.solvaysolexis.com.
26. Fürderer, T. Prozessoptimierung durch angepasste Oberflächen in der Chemiefaserverarbeitung [dissertation]. RWTH Aachen: Aachen, 2007. German.
27. Origin Lab. OringPro 8.1 Product Description. Origin Lab: Northampton. Available at http://www.originlab.com/.
28. Shawe, J. E. K.; Hütter, T.; Heitz, C.; Alig, I.; Lellinger, D. Thermochim Acta 2006, 446(1/2),147.
29. Auriemma, F.; Rosa, C.; Corradini, P. Adv Polym Sci 2005, 181, 1.